

Study of H^- Production in DC H^- Source of Medical Cyclotron*

Haruhiko ETOH, Moriaki ONAI¹⁾, Yasushi AOKI, Hitoshi MITSUBORI, Yoshihiko ARAKAWA, Junji SAKURABA, Takanori KATO, Toshinori MITSUMOTO, Satoru YAJIMA, Takanori SHIBATA²⁾, Akiyoshi HATAYAMA¹⁾ and Yoshikazu OKUMURA^{3, a)}

Sumitomo Heavy Industries, Ltd., Tokyo 141-6025, Japan

¹⁾Graduate School of Science and Technology, Keio University, Yokohama 223-8522, Japan

²⁾High Energy Accelerator Research Organization (KEK), Tsukuba 305-0801, Japan

³⁾Fusion Research and Development Directorate, Japan Atomic Energy Agency, Aomori 039-3212, Japan

(Received 30 November 2015 / Accepted 20 February 2016)

A filament driven multi-cusp negative hydrogen ion source has been developed for proton cyclotrons. In order to increase the H^- beam current, the dependences of H^- beam current on various design/operating parameters has been studied experimentally and numerically. In this paper, the effects of arc-discharge voltage and current on H^- production via the volume production process are investigated by three-dimensional kinetic modeling of electrons in the source plasma and zero-dimensional rate equations. This numerical analysis reproduces the experimental results of H^- beam current dependence on the arc-discharge condition, and also gives reasonable explanations for their characteristics.

© 2016 The Japan Society of Plasma Science and Nuclear Fusion Research

Keywords: negative hydrogen ion source, medical cyclotron, EEDF, KEIO-MARC code

DOI: 10.1585/pfr.11.2406063

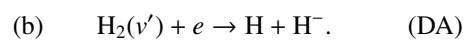
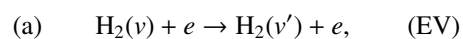
1. Introduction

Negative hydrogen ion (H^-) beam is widely used for medical proton cyclotrons, whose applications are cancer therapy and diagnostics, such as boron neutron capture therapy (BNCT) and the radioisotope production for molecular imaging technology. These applications require high intensity beam extracted from cyclotron to shorten the irradiation time for BNCT and increase the production rate of medical radioisotope.

A DC arc-discharge multi-cusp H^- source has been developed for improving the cyclotron's beam intensity. Since the addition of Caesium (Cs) into this type of source is known to increase the production rate of H^- on the surface of the plasma electrode [1], Cs-free and Cs-seeded operations have been tested on our source. 10 mA of H^- beam current has been obtained stably at an arc-discharge power of about 3 kW in the Cs-free operation [2], and H^- current has reached 22 mA at a lower arc-discharge power of 2.6 kW with less gas flow rate and fewer co-extracted electrons in the Cs-seeded operation [3].

In order to enhance H^- beam current, the relationship between the H^- production and the design/operating parameters of our source (such as arc-discharge power, magnetic field configuration, and so on) has been studied. The experimental results show the saturation of H^- beam current at higher arc power in the Cs-free operation

[2, 3]. Therefore, it is necessary to investigate the effects of the arc voltage (V_{arc}) and the arc current (I_{arc}) on the H^- production to improve H^- beam current. In the Cs-free operation, H^- ions are produced by the volume production process that consists of the following two-step reactions [4]:



The first reaction (a) is the vibrational excitation (EV) by the impact of the high energy electron (several tens of eV) on the H_2 molecule. The second reaction (b) is the H^- production via the dissociative attachment (DA) of the low energy electron (~ 1 eV) to the vibrationally excited molecule $H_2(v)$. The cross section of DA reaction becomes large at higher vibrationally excitation level ($v > 6$) [5]. In the present paper, the H^- production via these reactions at different arc-discharge conditions are investigated by the numerical analysis of electron energy distribution function (EEDF) in 3D3V (three-dimensional real and velocity) space and zero-dimensional (0D) rate equations for $H_2(v)$ and H^- densities. The high energy tail of the EEDF plays a key role for the efficient H^- volume production, because high energy electrons promote the EV reaction. Therefore, it is important to study the EEDF, especially the high-energy part of the EEDF. The EEDF analysis is conducted by KEIO-MARC code (Kinetic modeling of Electrons in the IOn source plasmas by the Multi-cusp ARC-discharge) [6–8]. There are several previous studies on modeling the volume production process that have

author's e-mail: haruhiko.eto@shi-g.com

* This article is based on the presentation at the 25th International Toki Conference (ITC25).

^{a)} Present affiliation: National Institute for Quantum and Radiological Science and Technology

provided the fundamental comprehensions of H^- production in the source [9–19]. These achievements and related works are summarized in Ref. 20. However, these studies have been conducted by 0D numerical models without the spatial distribution of electrons. The transport of electrons has been modeled by the simple global confinement time. In contrast, KEIO-MARC code can directly solve the electron trajectories in the three-dimensional (3D) real space to reproduce a more realistic physics in the source.

2. EEDF Analysis by KEIO-MARC

The geometrical model of our source is shown in Fig. 1. The source consists of a cylindrical plasma chamber made of copper, multi-cusp permanent magnets, and three electrodes system. These electrodes are a plasma electrode, an extraction electrode, and a grounded electrode. Dipole magnets called as filter magnets are located at the extraction region of the chamber to create the magnetic filter field [21] whose direction is perpendicular to the central axis of the chamber. The magnetic filter divides the chamber volume into high energy electron region (driver region) for the EV reaction, and low energy electron region (extraction region) for the DA reaction. The Z-axis is determined as the central axis of the chamber and its value Z is defined as the distance from the inner surface of the plasma electrode as shown in Fig. 1. The internal diameter and length of the chamber are 100 mm and 160 mm, respectively. Hydrogen plasma is generated by arc-discharge between two tungsten filaments and the chamber wall. The 3D calculation of magnetic cusp and filter fields is conducted by ANSYS software package [22]. Figure 2 shows the calculated magnetic field on the Z-axis. The peak value of the magnetic filter field is about 110 G at the plasma electrode's surface ($Z = 0$ mm). The other peak at the bottom side of the chamber ($120 \text{ mm} < Z < 160 \text{ mm}$) is due to the magnetic field generated by cusp magnets located under the filaments.

In KEIO-MARC code, the equations of motion for each electron is followed by Eq. (1),

$$m_e \frac{dv_e}{dt} = -e(v_e \times \mathbf{B}) + (\text{collision force}), \quad (1)$$

where m_e , v_e , and \mathbf{B} are the electron mass, velocity, the magnetic field, respectively. Equation (1) is solved by the leap-frog method [23], and Coulomb collision process between electrons is calculated by the binary collision method [24]. More than five hundred reactions between the electrons and the hydrogen species are modeled by the null collision method [25]. In Eq. (1), the electric field is not included because quasi-neutrality is assumed. Sheath potentials at the wall and the surface of the filaments are taken into account by simple models [8]. The initial energy of electron is set to be the same as the V_{arc} . The number of electrons emitted from the filaments is determined by the I_{arc} .

The number of test particles is set to be 1×10^4 . The

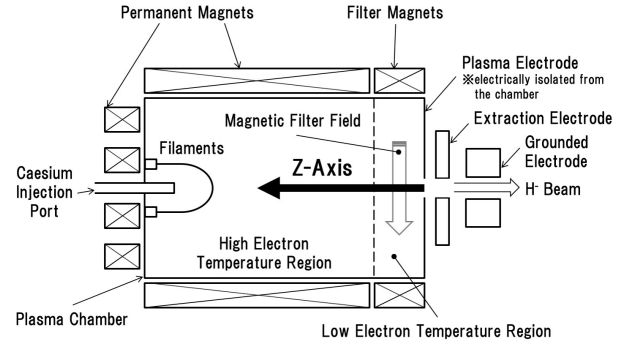


Fig. 1 The cross sectional view of the source.

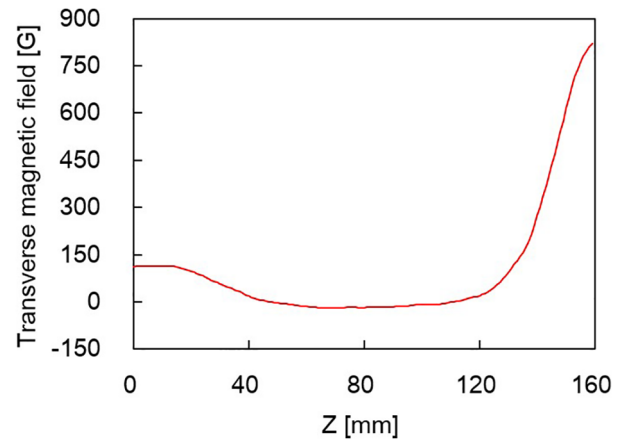


Fig. 2 The magnetic field on the Z-axis.

Table 1 Densities and temperatures of hydrogen species.

Hydrogen species	Density [m^{-3}]	Temperature [K]
H_2	1.49×10^{20}	774
H^0	1.49×10^{19}	1000
H^+	4.0×10^{17}	5700
H_2^+	1.0×10^{17}	1000
H_3^+	5.0×10^{17}	1000

hydrogen gas pressure is 1.6 Pa, which is estimated from the actual value of gas flow rate measured experimentally. Other parameters of neutral particles and ions, such as their gas temperatures and densities, are given from Ref. 4. These parameters are summarized in Table 1. The internal space of the chamber is divided into small cubic cells ($2 \text{ mm} \times 2 \text{ mm} \times 2 \text{ mm}$). The wall boundary is specified by the cell located at the chamber wall. The EEDF and the resultant electron density are calculated for each spatial cell with the number of test electrons and the cell-volume.

Figure 3 shows an EEDF dependence on the arc voltage V_{arc} at the driver region ($Z = 80 \text{ mm}$). The arc current I_{arc} is constant as 20 A. High energy tail of the EEDF is shifted toward the higher energy side as V_{arc} rises. Figure 4 shows an EEDF calculation results at $I_{\text{arc}} = 20 \text{ A}$ in the extraction region ($Z = 16 \text{ mm}$). The high energy electrons are reduced by the magnetic filter field in the extraction region. Figures 5 and 6 show an EEDF dependence on I_{arc} at

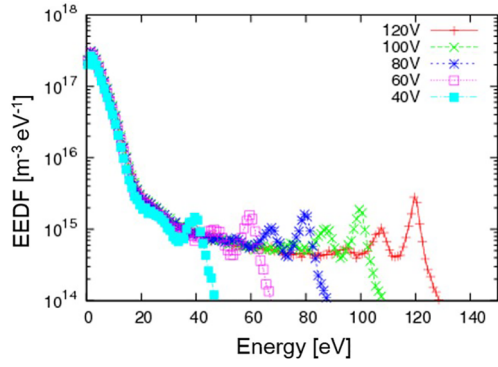


Fig. 3 EEDF dependence on arc voltage at the driver region (I_{arc} is 20 A).

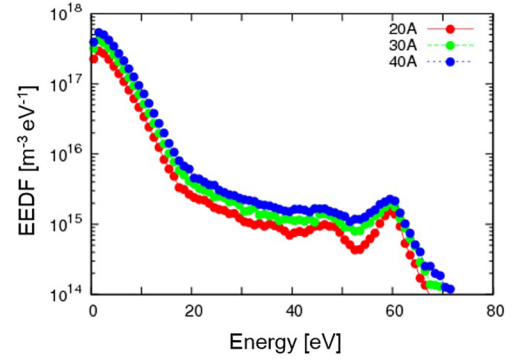


Fig. 5 EEDF dependence on arc current at the driver region (V_{arc} is 60 V).

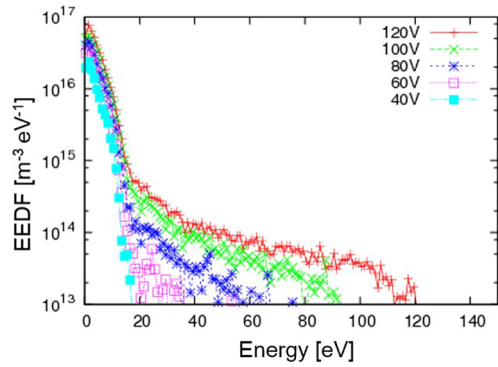


Fig. 4 EEDF dependence on arc voltage at the extraction region (I_{arc} is 20 A).

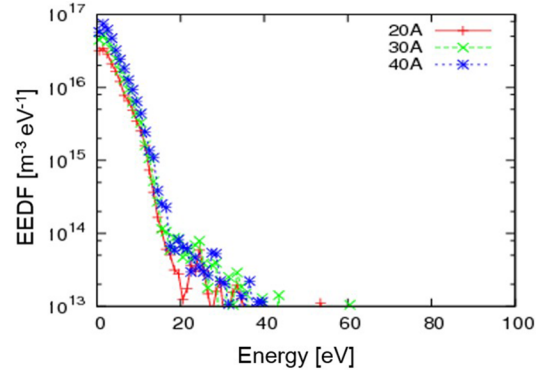


Fig. 6 EEDF dependence on arc current at the extraction region (V_{arc} is 60 V).

V_{arc} of 60 V in the driver region and the extraction region, respectively. These results show that I_{arc} does not change the high energy tail of the EEDF, but has a role to increase the number of electrons.

3. $\text{H}_2(v)$ Density

The $\text{H}_2(v)$ population density is calculated by rate equations for each vibrationally state ($0 \leq v \leq 14$)

$$\begin{aligned} \frac{dN(v)}{dt} = & N(e)N(v')R(eV; v' \rightarrow v) \\ & + N(e)N(v')R(EV; v' \rightarrow v) \\ & - N(e)N(v)R(eV; v \rightarrow v') \\ & - N(e)N(v)R(EV; v \rightarrow v') \\ & - N(e)N(v)R(\text{diss}; v) \\ & - N(e)N(v)R(\text{DA}; v) \\ & - N(v)N(\text{H}^+)R(\text{IC}; v) - \gamma \frac{N(v)}{\tau} + S, \quad (2) \end{aligned}$$

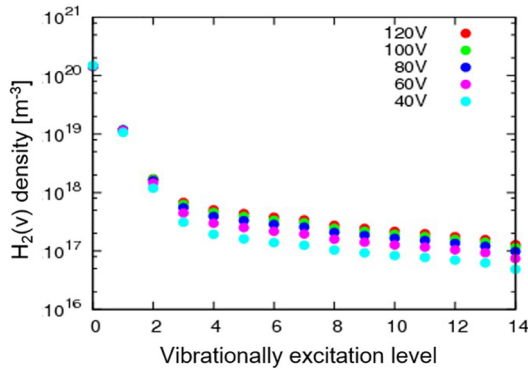
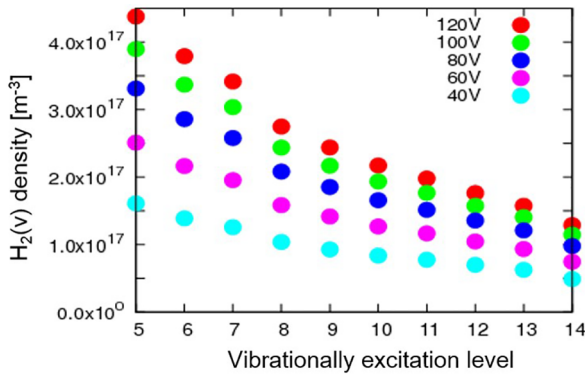
where $N(e)$ is the electron density, $N(v)$ and $N(v')$ are densities of hydrogen molecules at different vibrationally excitation levels v and v' respectively. In addition, $N(\text{H}^+)$

is the H^+ density, γ and τ are the reflection rate of vibrationally excited hydrogen molecules at the wall boundary and their confinement time, respectively. Finally, S is the neutral source determined by the gas flow rate. The electron density $N(e)$ is calculated from the EEDF at the driver region. In Eq. (2), $N(\text{H}^+)$ is adjusted to be equal to $N(e)$, so as to keep the charge neutrality at each spatial cell. The reactions taken into account in the analysis are listed in Table 2. The reaction rate coefficients R in Eq. (2) are calculated from the cross section data from the references in Table 2 and the EEDF at the driver region. The confinement time τ is calculated as L/v_{H_2} , where L is the radius of the plasma chamber and v_{H_2} is the average velocity of H_2 molecules. γ is the parameter given parametrically [9], and is set to be 0.8 in the analysis.

Figure 7 shows the dependence of $\text{H}_2(v)$ density on V_{arc} at each excitation level. The arc current I_{arc} is 20 A in this analysis. As shown in Fig. 7, The $\text{H}_2(v)$ density increases with V_{arc} increasing. This is caused by the increase in the high energy tail of the EEDF with V_{arc} as shown in Fig. 3. Figure 8 shows same data from Fig. 7 replotted with a linear scale, the $\text{H}_2(v)$ density saturates at higher V_{arc} due to the $\text{H}_2(v)$ destruction caused by high energy electrons. Figure 9 shows the dependence of $\text{H}_2(v)$ density on I_{arc} at $V_{\text{arc}} = 60$ V. As seen from Fig. 9, the population density of $\text{H}_2(v)$ does not depend so much on I_{arc} . These results show

Table 2 Reactions taken account in Eqs. (2) and (3).

	Reaction	Ref.
eV	$e + \text{H}_2(\text{X}^1\Sigma_g^+; v) \rightarrow e + \text{H}_2(\text{X}^1\Sigma_g^+; v' = v \pm 1)$	[26]
EV	$e + \text{H}_2(\text{X}^1\Sigma_g^+; v) \rightarrow e + \text{H}_2(\text{C}^1\Pi_u)$ $\rightarrow e + \text{H}_2(\text{X}^1\Sigma_g^+; v')$	[26]
EV	$e + \text{H}_2(\text{X}^1\Sigma_g^+; v) \rightarrow e + \text{H}_2(\text{B}^1\Pi_u)$ $\rightarrow e + \text{H}_2(\text{X}^1\Sigma_g^+; v')$	[26]
Diss	$e + \text{H}_2(\text{X}^1\Sigma_g^+; v) \rightarrow e + \text{H}_2(\text{b}^3\Sigma_u^+)$ $\rightarrow e + \text{H}(1s) + \text{H}(1s)$	[26]
DA	$\text{H}_2(v) + e \rightarrow \text{H}^- + \text{H}$	[27]
IC	$\text{H}^+ + \text{H}_2(v) \rightarrow \text{H}(1s) + \text{H}_2^+$	[28]
ED	$\text{H}^- + e \rightarrow \text{H}(1s) + e + e$	[28]
MN	$\text{H}^- + \text{H}^+ \rightarrow \text{H} + \text{H}(1s)$	[28]
AD	$\text{H}_2^+ + e \rightarrow \text{H}(1s) + e + e$	[28]

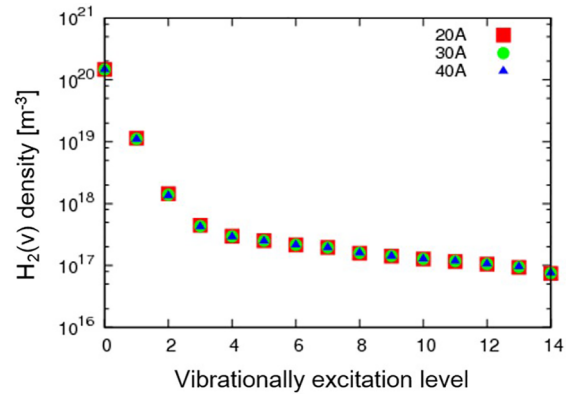
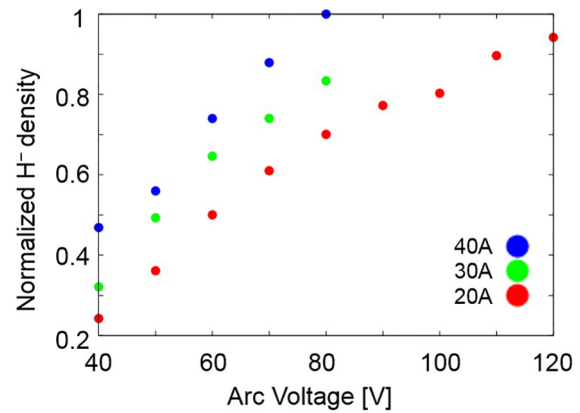

 Fig. 7 $\text{H}_2(v)$ density at each vibrationally excitation level for different arc voltages (I_{arc} is 20 A).

 Fig. 8 $\text{H}_2(v)$ density at each vibrationally excitation level ($5 \leq v \leq 14$) from Fig. 7 replotted with a linear scale.

that the high energy tail of the EEDF mainly enhance the population density of $\text{H}_2(v)$ with the relatively high vibrationally excited number ($v > 4$).

4. H^- Density

The H^- density is calculated by the rate equation at the steady state [29]

$$N(\text{H}^-) = \frac{N(e)N(v)R(\text{DA}; v)}{N(\text{H}^+)R(\text{MN}) + N(\text{H})R(\text{AD}) + N(e)S(\text{ED}) + \frac{1}{\tau}}, \quad (3)$$


 Fig. 9 $\text{H}_2(v)$ density at each vibrationally excitation level for different arc currents (V_{arc} is 60 V).

 Fig. 10 Normalized H^- density as a function of arc voltage calculated by Eq. (3).

where $N(\text{H}^-)$ and $N(\text{H}^+)$ are the H^- density and the H^+ density, respectively. In Eq. (3), $N(e)$ is given by the EEDF at the extraction region, while $N(v)$ is given by the $\text{H}_2(v)$ density discussed in the previous section.

Figure 10 shows the H^- density as a function of V_{arc} for different $I_{\text{arc}} = 20 \text{ A}$, 30 A , and 40 A . Figure 11 shows the H^- beam current measured at the Faraday Cup as a function of V_{arc} . In both figures, data points are normalized by the values of the maximum H^- density and beam current ($V_{\text{arc}} = 80 \text{ V}$, $I_{\text{arc}} = 40 \text{ A}$). The simulation result of the H^- density reproduces the H^- beam current dependences on V_{arc} and I_{arc} obtained experimentally. In the simulation result, the H^- density is increased by V_{arc} and saturates at higher V_{arc} . These characteristics are possibly explained by the $\text{H}_2(v)$ density dependences on V_{arc} . The H^- density is also increased with I_{arc} , which is caused mainly by the enhancement of the DA reaction, because I_{arc} increases the low energy electrons at the extraction region as shown in Fig. 6, and does not change the $\text{H}_2(v)$ density as shown in Fig. 9.

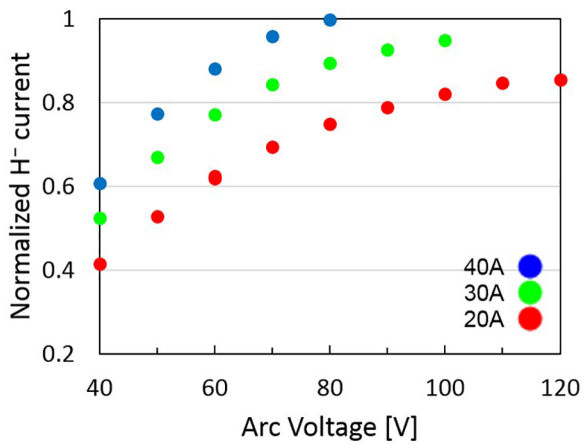


Fig. 11 Normalized H⁻ beam current as a function of arc voltage obtained experimentally.

5. Conclusion

The numerical study of H⁻ production via the volume production process gives the reasonable explanation of the H⁻ beam current dependencies on V_{arc} and I_{arc} obtained experimentally. Arc voltage has a role to enhance high energy tail of the EEDF, which promotes $\text{H}_2(\nu)$ production through the EV reaction. Because of this enhancement of $\text{H}_2(\nu)$, H⁻ density increases with V_{arc} . The saturation of H⁻ density is due to the $\text{H}_2(\nu)$ destruction caused by high energy electrons. On the other hand, I_{arc} does not change the high energy tail of the EEDF but increase the number of electrons. The increase in low energy electrons at the extraction region enhances the H⁻ production through the DA reaction.

- [1] S.R. Walther, K.N. Leung and W.B. Kunkel, *J. Appl. Phys.* **64**, 3424 (1988).
- [2] H. Etoh *et al.*, *Rev. Sci. Instrum.* **85**, 02B107 (2014).
- [3] H. Etoh *et al.*, *Rev. Sci. Instrum.* **87**, 02B135 (2016).
- [4] M. Bacal *et al.*, *J. Appl. Phys.* **52**, 1247 (1981).
- [5] J.M. Wadehra and J. N. Bardsley, *Phys. Rev. Lett.* **41**, 1795 (1978).
- [6] T. Shibata, M. Kashiwagi, T. Inoue, A. Hatayama and M. Hanada, *J. Appl. Phys.* **114**, 143301 (2013).
- [7] I. Fujino, A. Hatayama, N. Takado and T. Inoue, *Rev. Sci. Instrum.* **79**, 02A510 (2008).
- [8] R. Terasaki, I. Fujino, A. Hatayama, T. Mizuno and T. Inoue, *Rev. Sci. Instrum.* **81**, 02A703 (2010).
- [9] J.R. Hiskes, A.M. Karo, M. Bacal, A.M. Bruneteau and W.G. Graham, *J. Appl. Phys.* **53**, 3469 (1982).
- [10] J.R. Hiskes and A.M. Karo, *J. Appl. Phys.* **56**, 7, 1927 (1984).
- [11] J.R. Hiskes, A.M. Karo and P.A. Willmann, *J. Appl. Phys.* **58**, 5, 1759 (1985).
- [12] J. Bretagne, G. Delouya, C. Gorse, M. Capitelli and M. Bacal, *J. Appl. Phys. D: Appl. Phys.* **18**, 811 (1985).
- [13] O. Fukumasa and S. Saeki, *J. Phys. D: Appl. Phys.* **18**, L21 (1985).
- [14] J. Bretagne, G. Delouya, M. Capitelli, C. Gorse and M. Bacal, *J. Phys. D: Appl. Phys.* **19**, 1197 (1986).
- [15] C. Gorse, M. Capitelli, M. Bacal, J. Bretagne and A. Laguna, *Chem. Phys.* **117**, 177 (1987).
- [16] M. Ohmatsu, K. Shimura and M. Ogasawara, "Role of magnetic filter in the tandem type negative ion source," in *Proc. 11th Symp. Ion Sources Ion-Assisted Technol.*, Tokyo, Japan, Jun. 1-3, 1987, pp.183-186.
- [17] O. Fukumasa, *J. Phys. D: Appl. Phys.* **22**, 1668 (1989).
- [18] O. Fukumasa and S. Ohashi, *J. Phys. D: Appl. Phys.* **22**, 1931 (1989).
- [19] M. Ogasawara, M. Ohmatsu, T. Kawamura, K. Shimura and T. Yamakawa, "Modeling of magnetic filter in zero-dimensional code for tandem negative ion source," in *Proc. 13th Symp. Ion Sources Ion-Assisted Technol.*, Tokyo, Japan, Jun. 1-3, 1990, pp.83-88.
- [20] M. Bacal, A. Hatayama and J. Peters, *IEEE Trans. Plasma Sci.* **33**, 6, 1845 (2005).
- [21] K.N. Leung, K.W. Ehlers and M. Bacal, *Rev. Sci. Instrum.* **54**, 56 (1983).
- [22] Ansys homepage (2015) (<http://www.ansys.com/>)
- [23] C.K. Birdsall *et al.*, in *Plasma Physics via Computer Simulation*, (IOP Publishing, Bristol, 1991), Chap. 2, pp.12-15.
- [24] T. Takizuka *et al.*, *J. Comput. Phys.* **25**, 205 (1977).
- [25] K. Nanbu *et al.*, in *Proc. Soviet Union-Japan Symp. Comput. Fluid Dynamics*, (Computing Center of the USSR Academy of Sciences, 1989), Vol.2, pp.126-132.
- [26] R. Celiberto *et al.*, *At. Data Nucl. Data Tables* **77**, 161 (2001).
- [27] R.K. Janev *et al.*, *Julich Report No. JUEL-4105*, 2003.
- [28] P.T. Grennland *et al.*, *Julich Report No. JUEL-3528*, 1996.
- [29] C. Courteille *et al.*, *Rev. Sci. Instrum.* **64**, 3265 (1993).